Electronic Supplementary Material (ESI) for Chemical Science.
This journal is © The Royal Society of Chemistry 2022

Supplementary Information

Materials and methods

Chemicals

Commercial iridium oxide hydrate catalyst ($IrO_2 \cdot xH_2O$, 99.95% trace metals), titanium carbide (nanopowder, particle size < 200 nm), ruthenium(IV) oxide (RuO_2, 99.95% trace metals), ruthenium black, perchloric acid ($HClO_4$, 99.99% trace metal basis), iridium(III) chloride ($IrCl_3 \cdot xH_2O$, 99.9% trace metal basis), ruthenium(III) chloride ($RuCl_3$, Ru content 45-55 wt.%), potassium hydroxide (KOH, ≥99.99% trace metals basis), isopropyl alcohol (IPA, ≥99.5 wt.%), ethylene glycol (ReagentPlus®, ≥99 wt.%), copper sulfate ($CuSO_4$, ReagentPlus®, ≥99 wt.%), and sulfuric acid (H_2SO_4, ACS reagent, 95.0-98.0 wt.%) were purchased from Sigma-Aldrich. Iridium black (99.95% trace metals basis) was obtained from Alfa Aesar. Nafion dispersion (5 wt.%, alcohol-based) was purchased from Fuel Cell Store (Texas, USA). All chemicals were used without further purification. Ultrapure water (18 MΩ/cm) used in all experiments was prepared by the Millipore system.

Synthesis of Ir_xRu_y/TiC

In a typical synthesis, iridium(III) chloride hydrate, ruthenium(III) chloride, and 200 mg of TiC were dissolved in 50 mL ethylene glycol at room temperature in a beaker. The loading of Ir and Ru was set at 20 wt. % relative to TiC. The obtained mixture was stirred for 1 hour at a rotation speed of 800 rpm to form a uniform suspension. Subsequently, the suspension was heated over an oil bath filled with silicon oil for 5 hours at the same rotating speed and 170 °C. After the reaction, the product was washed with deionized water 5 times and harvested using a centrifuge, and then dried in a vacuum oven.

Physical characterization

X-ray diffraction (XRD) was performed on a Shimadzu XRD-6000 with Cu Kα radiation (40 kV, 30 mA, λ = 1.5418Å). The morphological and structural information was examined by a JEOL JEMARM200F scanning transmission electron microscopy (STEM) with sub-angstrom-resolution (0.08 nm) equipped with an energy-dispersive X-ray spectroscopy (EDX) analyzer. Atomic resolution images were taken in the high-angle annular dark-field (HAADF–STEM) mode. Electron energy loss spectroscopy (EELS) spectra were collected using a Gatan imaging filter (Quantum 965).

X-ray absorption spectroscopy (XAS) was carried out in total-fluorescence-yield mode at ambient air with beamline of BL-12B2 ($25 < E < 70$ keV, with a resolution of $\Delta E/E \sim 10^{-4}$) in Spring-8, HARSI, Japan. X-ray absorption near-edge structure (XANES) and extended X-ray absorption fine structure

(EXAFS) were performed to examine the valence state and coordination environment. Energy scan range between 11,000 and 12,000 eV was used to measure the Ir spectra, and energy scan range between 21,800 and 22,800 eV was used to measure the Ru spectra. The wavelet transform of the EXAFS spectra was based on the Continuous Cauchy Wavelet Transform (CCWT) modulus.[1, 2] The coordination fitting of EXAFS spectra was conducted by Athena software using the standard crystal structure file from American Mineralogist Crystal Structure Database.

Electrochemical measurements

The OER performance of the as-prepared samples was measured in 0.1 M ultrapure $HClO_4$ solution based on a three-electrode configuration. A leak-free saturated calomel electrode (SCE) was used as the reference electrode and a Pt plate was used as the counter electrode. The electrochemical performance was examined on a glassy carbon rotating disk electrode (RDE, disk diameter = 5.5 mm, Pine Research Instrument). All electrochemical data were collected on a CHI 760e electrochemical workstation (CH instrument). The loading amount of catalyst was kept as 100 μg/cm^2. The OER polarization curves were measured in N_2 saturated 0.1 M ultrapure $HClO_4$ solution at a scan rate of 5 mV/s with a rotating speed of 1600 rpm. The current density was normalized to the electrode area of glassy carbon (GC). The stability tests were performed in 0.1 M $HClO_4$ solution at 10 mA/cm^2.

The surface structure of Ir_xRu_y/TiC after OER was characterized by electrochemical Cu stripping. The Ir_xRu_y/TiC sample was first electrochemically reduced in 0.1 M H_2SO_4 solution at 0.02 V vs. SCE and then moved into a mixed solution containing 0.05 M H_2SO_4 and 1 mM $CuSO_4$ with potential held at 0.02 V vs. SCE for 100 s.[2] Afterwards, the catalyst was transferred into a Cu-free electrolyte and a cyclic voltammetry measurement was conducted.

Computational details

A 2×2×1 supercell of bulk Ru with different ratios of Ir was used to model IrRu alloy. The calculated bulk structures and lattice parameters are shown in **Table S4**. Then the (101) surface of the expanded 2×2×2 supercell was built to simulate the IrRu alloy before electrocatalysis. The selected parameters of (101)-surface structures for Ir_1Ru_3, Ir_1Ru_1, Ir_3Ru_1 and Ir are listed in **Table S5**. The slab consists of four atomic layers, where the bottom two were frozen while the remaining layers were allowed to relax. As shown in the experimental results (Figure 2e, S5 and Table S3), the surface was covered with Ir oxide while surface Ru had been etched into the solution during OER. Therefore, we built an IrO_x cluster anchored on the (101)-surface of Ir_xRu_y alloy with different Ir/Ru ratios to simulate the real active surfaces, as shown in **Figure S8**. All the supercell slabs were repeated periodically with a 15 Å vacuum layer between the images in the direction of the surface normal.

All DFT calculations were performed by using the spin-polarized Kohn-Sham formalism with the generalized gradient approximation (GGA) of Perdew-Burke-Ernzerhof (PBE),[3] as implemented in the Vienna Ab-initio Simulation Package (VASP version 5.4.4).[4] The valence electronic states of all atoms were expanded in a plane-wave basis set with a cutoff energy of 400 eV, and a Monkhorst-Pack 3×3×1 grid was used to sample the Brillouin zone. Atomic positions were optimized by using a conjugate gradient algorithm until the forces were less than 0.03 eV $Å^{-1}$ for all intermediates. Vibrational frequency analysis was performed and Gibbs free energy corrections were calculated by using VASPKIT 1.2.5.[5]

Supplementary figures

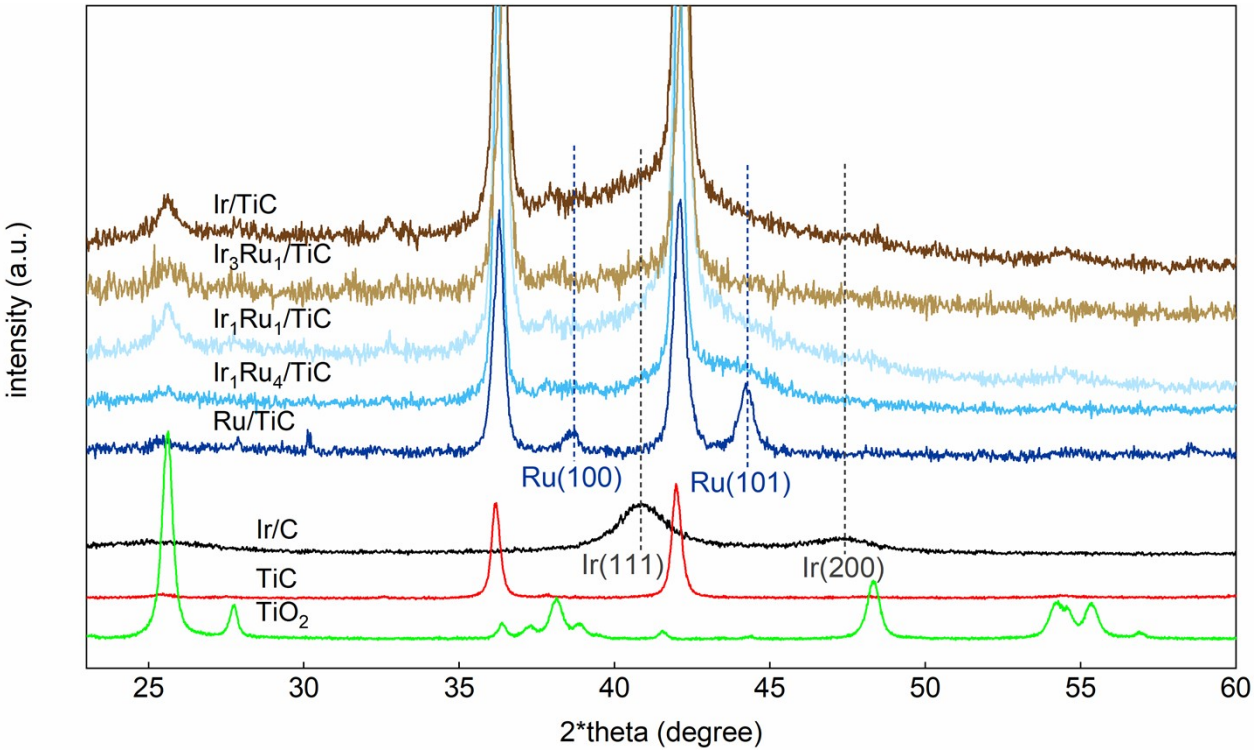

Figure S1. X-ray diffraction patterns of Ir_xRu_y/TiC with different Ir/Ru ratios.

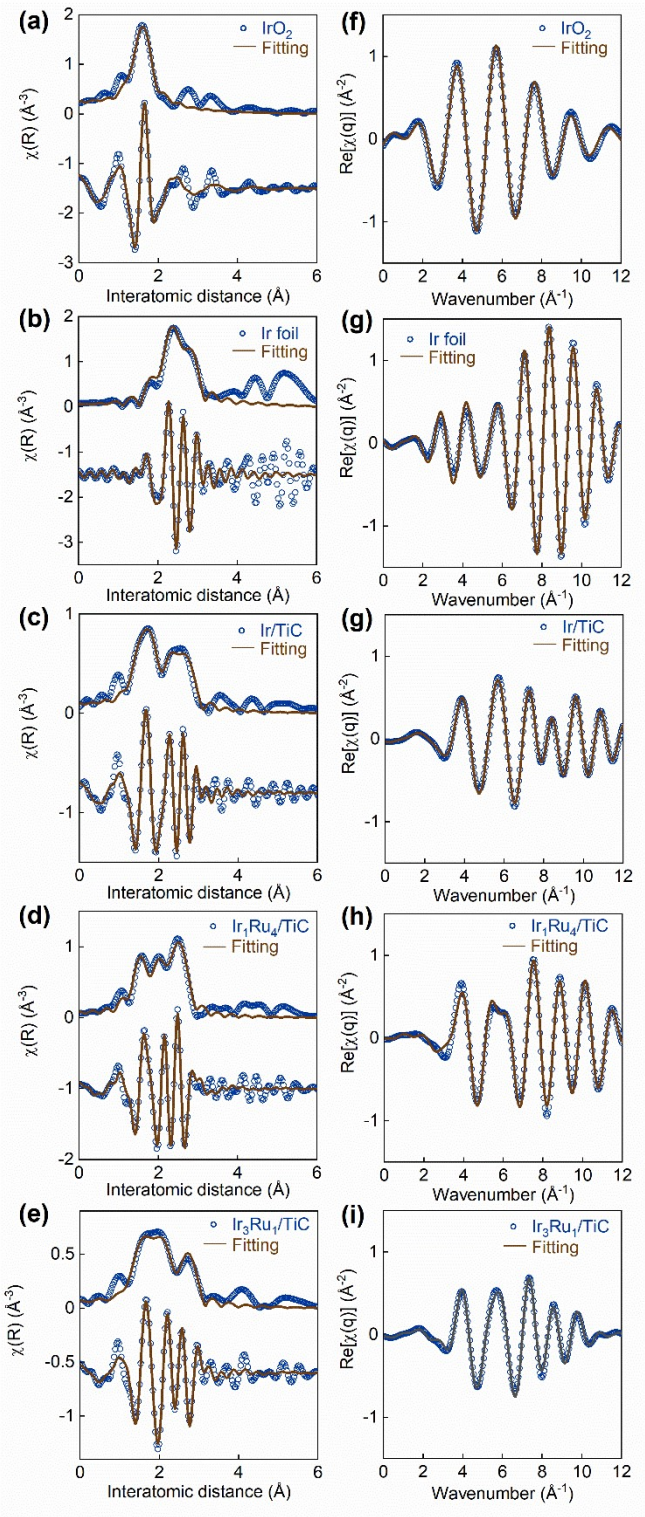

Figure S2. EXAFS fitting of Ir/TiC, IrO_2, $IrRu_4$/TiC, Ir_3Ru_1/TiC, and Ir foil. Left column: k2-weighted q-space spectra. Right column: k2-weighted k-space spectra.

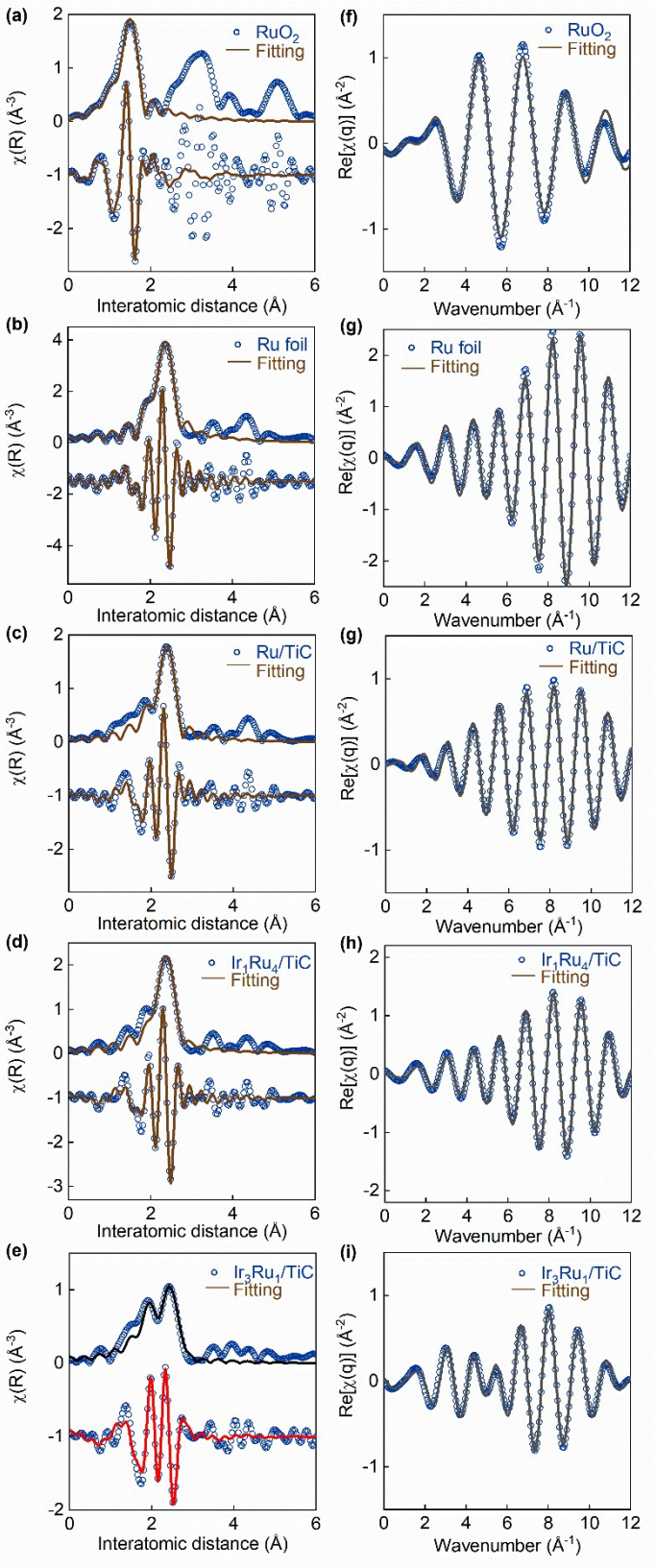

Figure S3. EXAFS fitting of Ru/TiC, RuO_2, $IrRu_4$/TiC, Ir_3Ru_1/TiC, and Ru foil. Left column: k2-weighted q-space spectra. Right column: k2-weighted k-space spectra.

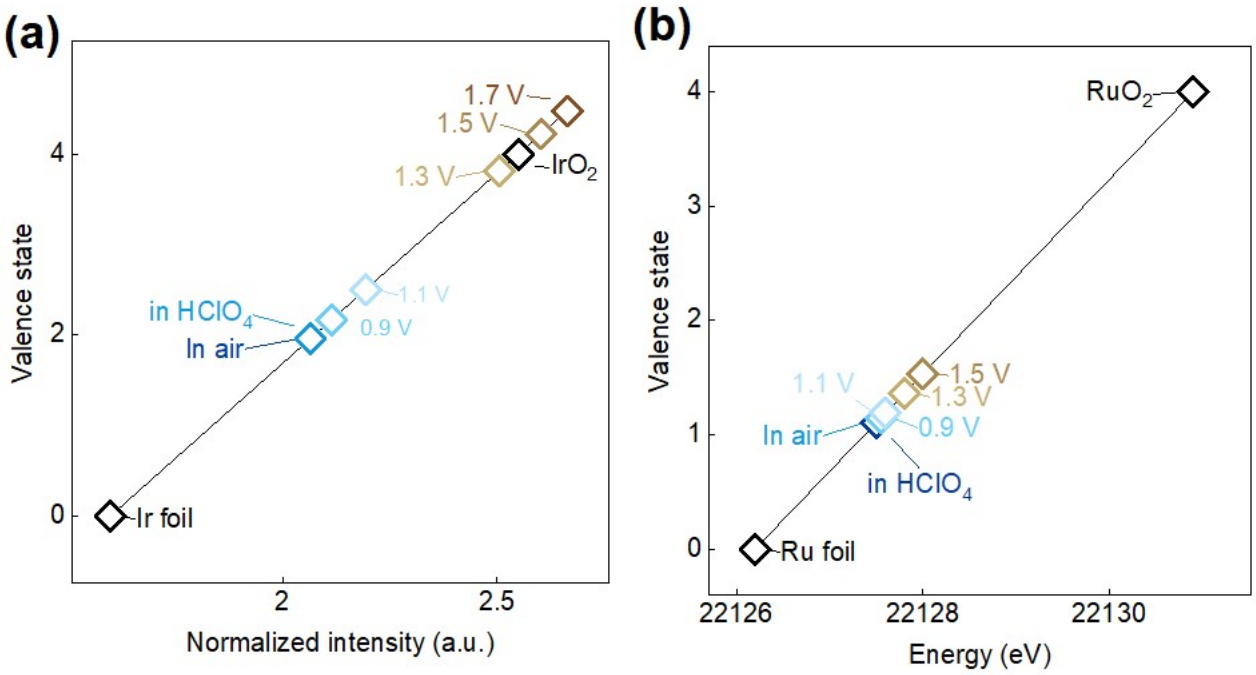

Figure S4. Normalized valence state change of (a) Ir and (b) Ru quantified from *in situ* EXAFS on Ir_1Ru_4/TiC for acidic OER.

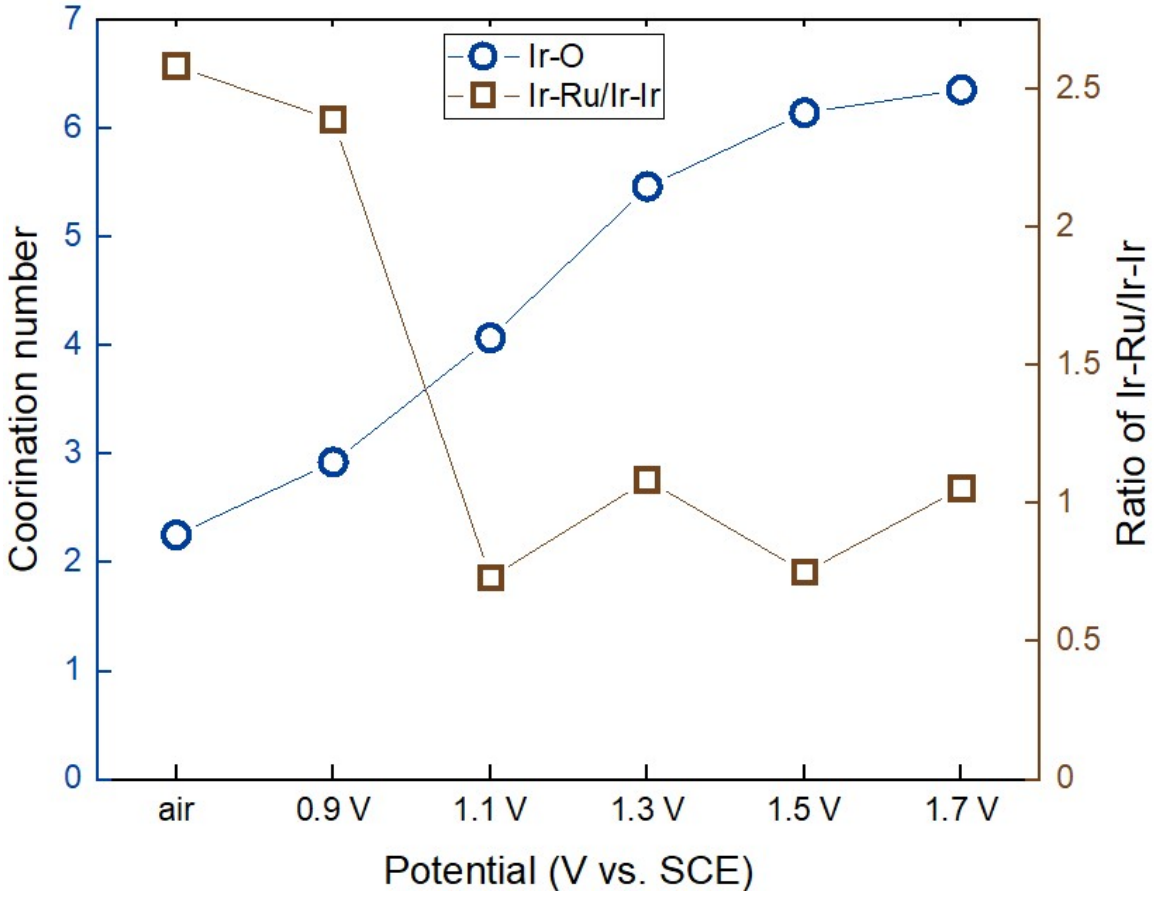

Figure S5. Evolution of Ir-O coordination and Ir-Ru/Ir-Ir ratio in Ir_1Ru_4/TiC as a function of applied potential.

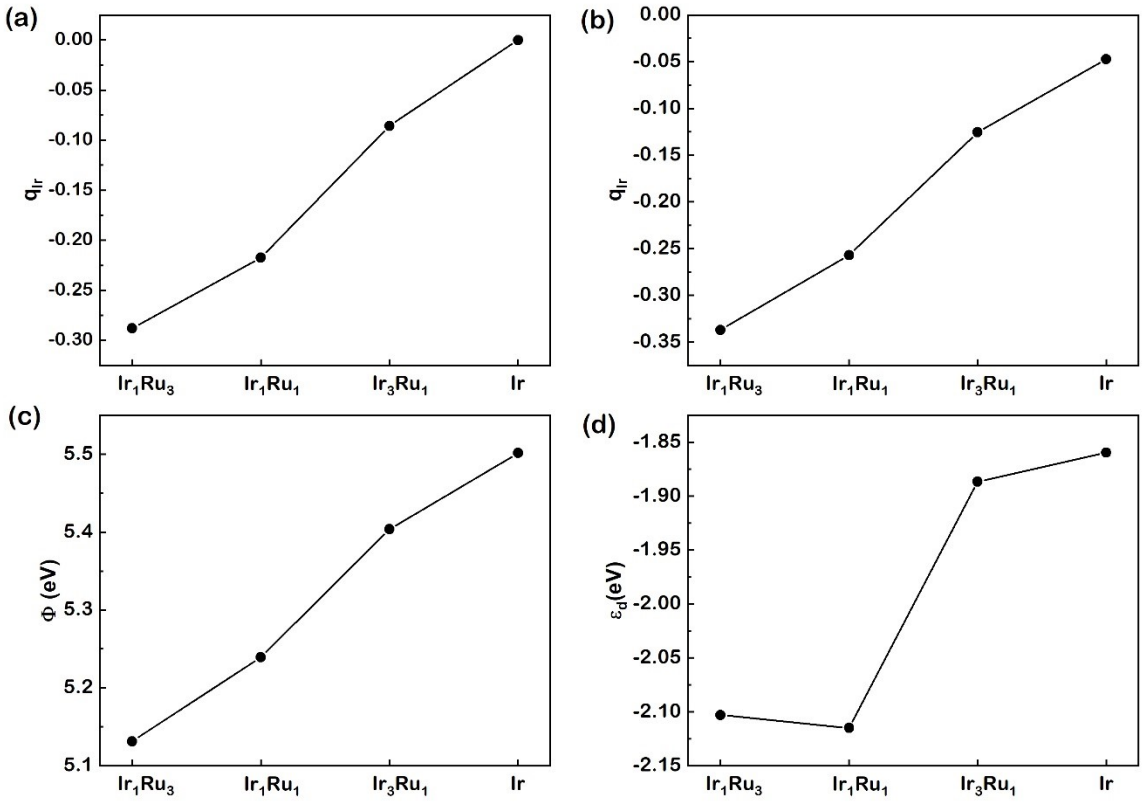

Figure S6. Bader charge of Ir atom for bulk (**a**) and (101)-surface (**b**) of Ir_1Ru_3, Ir_1Ru_1 and Ir_3Ru_1 alloy. (**c**) Work-function of (101)-surface for Ir_1Ru_3, Ir_1Ru and Ir_3Ru alloy. (**d**) *d*-band center of Ir atom on (101)-surface of Ir_1Ru_3, $IrRu_1$ and Ir_3Ru_1 alloy.

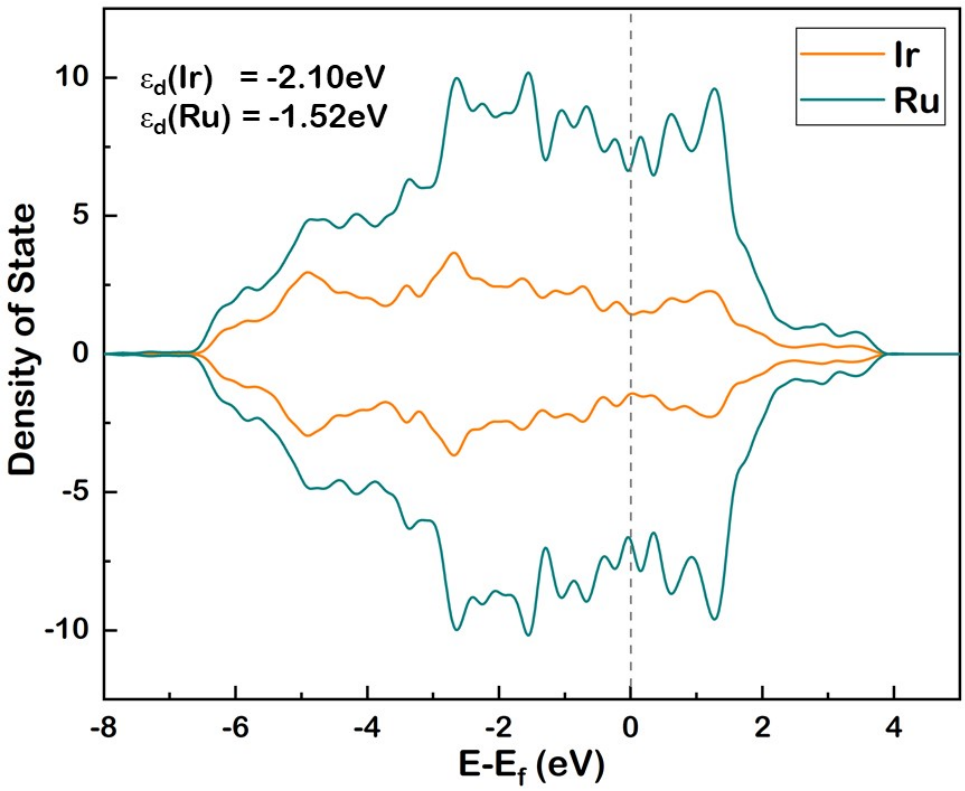

Figure S7. The projected density of state (pDOS) of surface Ru and Ir atoms for the $Ir_1Ru_3(101)$ model.

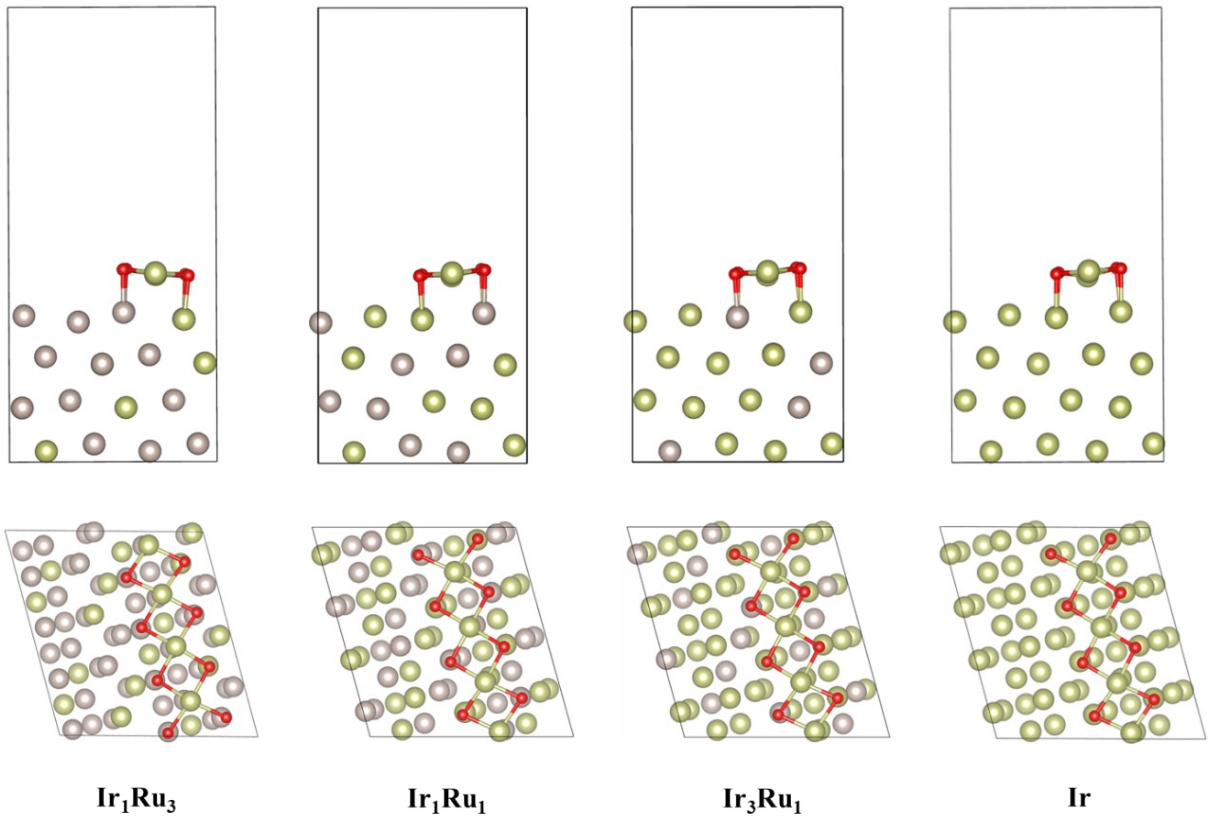

Figure S8. The computational models of $IrRu_3$, IrRu, Ir_3Ru and Ir for OER. The green, brown, and red spheres represent Ir, Ru and O, respectively.

Supplementary tables

Table S1. Structural parameters of IrO_2, Ir black, Ir/TiC, Ir_1Ru_4/TiC, and Ir_3Ru_1/TiC extracted from the EXAFS fitting for Ir centered scattering path ($^aS_0^2$=0.847).

Sample	Scattering pair	^{b}CN	$^d\sigma^2$(Å^2)	$^e\Delta E_0$(eV)	^{f}R factor	^{c}R(Å)
IrO_2	Ir-O	6*	0.00539	12.164	0.0377	1.9981
Ir	Ir-Ir	12*	0.00375	8.226	-0.01098	2.70392
Ir/TiC	Ir-O	2.731	0.00507	10.991	0.04539	2.00579
	Ir-Ir	4.926	0.00496	7.853	-0.03025	2.68466
Ir_1Ru_4/TiC	Ir-O	2.652	0.00628	6.286	0.00182	1.96222
	Ir-Ir	1.279	0.00032	6.286	-0.06567	2.64923
	Ir-Ru	3.543	0.00298	6.286	-0.02006	2.66324
Ir_3Ru_1/TiC	Ir-O	1.967	0.00621	2.981	-0.00766	1.95274
	Ir-Ir	6.31	0.00621	2.981	-0.08126	2.64784
	Ir-Ru	1.561	0.00621	2.981	-0.09487	2.63593

$^aS_0^2$ is the amplitude reduction factor (obtained by the fitting of Ir foil and IrO_2);

^{b}CN is the coordination number;

^{c}R is the interatomic distance (the bond length between Ir central atoms and surrounding coordination atoms);

$^d\sigma^2$ is Debye-Waller factor (a measure of thermal and static disorder in absorber-scatterer distances);

$^e\Delta E_0$ is edge-energy shift (the difference between the zero kinetic energy of the sample and that of the theoretical model);

^{f}R factor is used to evaluate the goodness of fitting;

*This value was fixed during EXAFS fitting, based on the known structure of Ir metal and bulk IrO_2.

Table S2. Structural parameters of Ru black, RuO_2, Ir_1Ru_4/TiC, Ir_3Ru_1/TiC, and Ru/TiC extracted from the EXAFS fitting for Ru centered scattering path ($^aS_0^2$=0.85).

Sample	Scattering pair	^{b}CN	$^d\sigma^2$(Å^2)	$^e\Delta E_0$(eV)	^{f}R factor	^{c}R(Å)
Ru	Ru-Ru_1	6*	0.01459	-7.371	-0.01703	2.63257
	Ru-Ru_2	6*	4E-4	-7.371	-0.03542	2.66847
RuO_2	Ru-O	6*	0.00193	-1.306	0.03382	1.97642
Ir_1Ru_4/TiC	Ru-Ru	8.602	0.00584	-19.826	-0.05364	2.68606
Ir_3Ru_1/TiC	Ru-Ru	5.857	0.00597	-19.308	-0.03376	2.70594
	Ru-Ir	5.8	0.0069	-20	-0.01972	2.71998
Ru/TiC	Ru-Ru	6.66	0.00557	-6.333	0.03624	2.68584

$^aS_0^2$ is the amplitude reduction factor (obtained by the fitting of Ru foil and RuO_2);

^{b}CN is the coordination number;

^{c}R is the interatomic distance (the bond length between Ir central atoms and surrounding coordination atoms);

$^d\sigma^2$ is Debye-Waller factor (a measure of thermal and static disorder in absorber-scatterer distances);

$^e\Delta E_0$ is edge-energy shift (the difference between the zero kinetic energy of the sample and that of the theoretical model);

^{f}R factor is used to evaluate the goodness of fitting;

*This value was fixed during EXAFS fitting, based on the known structure of Ru metal and bulk RuO_2.

Table S3. Structural parameters of Ir_1Ru_4/TiC extracted from the *in situ* EXAFS fitting for Ir centered scattering path ($^aS_0^2$=0.85).

Sample	Scattering pair	^{b}CN	$^d\sigma^2$(Å^2)	$^e\Delta E_0$(eV)	^{f}R factor	^{c}R(Å)	Figure
In air at OCP	Ir-O	2.256	0.0034	7.033	-0.05263	1.98067	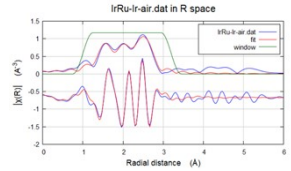
	Ir-Ir	1.118	-0.00215	7.033	-0.07325	2.65066	
	Ir-Ru	2.888	0.0012	7.033	-0.06134	2.66246	
0.9 V (vs. RHE)	Ir-O	2.928	0.00453	10.079	-0.0324	2.0009	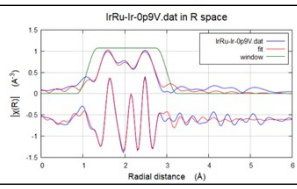
	Ir-Ir	1.637	0.00453	33.153	0.07394	2.79784	
	Ir-Ru	3.911	0.00453	10.079	-0.03568	2.68812	
1.1 V (vs. RHE)	Ir-O	4.07	0.00605	8.461	-0.06198	1.97132	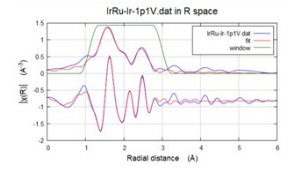
	Ir-Ir	2.333	0.00605	-10.936	-0.2562	2.4677	
	Ir-Ru	1.707	0.00605	8.461	-0.02437	2.69943	
1.3 V (vs. RHE)	Ir-O	5.466	0.00609	9.051	-0.06672	1.96658	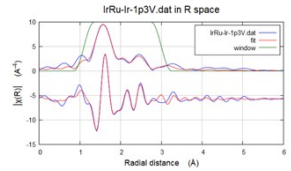
	Ir-Ir	1.541	0.00609	35.433	0.09268	2.81658	
	Ir-Ru	1.671	0.00609	9.051	-0.03846	2.68534	
1.5 V (vs. RHE)	Ir-O	6.148	0.0068	8.181	-0.07398	1.95932	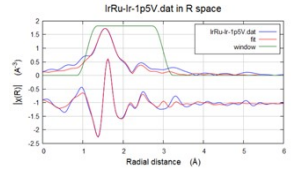
	Ir-Ir	1.781	0.0068	37.982	0.13136	2.85526	
	Ir-Ru	1.338	0.0068	8.181	-0.03583	2.68797	
1.7 V (vs. RHE)	Ir-O	6.359	0.00679	8.985	-0.06483	1.96847	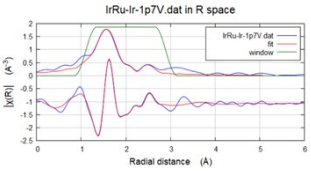
	Ir-Ir	1.697	0.00679	-2.524	-0.29167	2.43223	
	Ir-Ru	1.79	0.00679	-2.524	-0.01037	2.71343	

$^aS_0^2$ is the amplitude reduction factor (obtained by the fitting of Ir foil and IrO_2);

^{b}CN is the coordination number;

^{c}R is the interatomic distance (the bond length between Ir central atoms and surrounding coordination atoms);

$^d\sigma^2$ is Debye-Waller factor (a measure of thermal and static disorder in absorber-scatterer distances);

$^e\Delta E_0$ is edge-energy shift (the difference between the zero kinetic energy of the sample and that of the theoretical model);

^{f}R factor is used to evaluate the goodness of fitting;

*This value was fixed during EXAFS fitting, based on the known structure of Ir metal and bulk IrO_2.

Table S4. The calculated bulk structures and lattice parameters for IrRu alloy. The green and brown spheres represent Ir and Ru, respectively.

Model	Structure	Lattice Parameters
Ir_1Ru_3	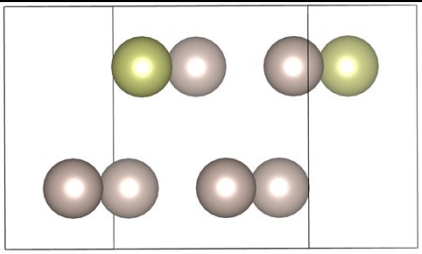	A = B = 5.454 Å C = 4.311 Å α = β = 90° γ = 120°
Ir_1Ru_1	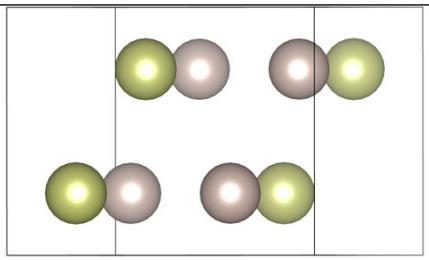	A = B = 5.478 Å C = 4.341 Å α = β = 90° γ = 120°
Ir_3Ru_1	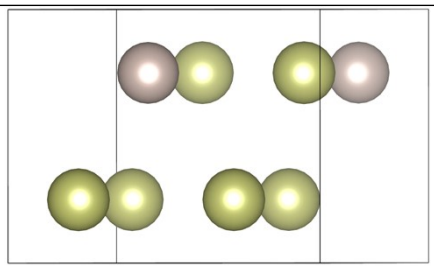	A = B = 5.486 Å C = 4.398 Å α = β = 90° γ = 120°

Table S5. The selected parameters of (101)-surface structures for Ir_1Ru_3, Ir_1Ru_1, Ir_3Ru_1 and Ir. The green and brown spheres represent Ir and Ru, respectively.

Model	Structure	Lattice Parameters
$Ir_1Ru_3(101)$	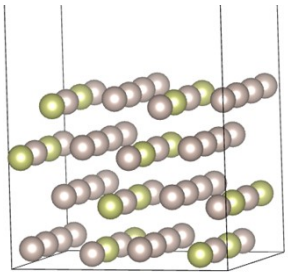	A = 10.203 Å B = 10.909 Å C = 21.564 Å α = 90° β = 90° γ = 105.52°
$Ir_1Ru_1(101)$	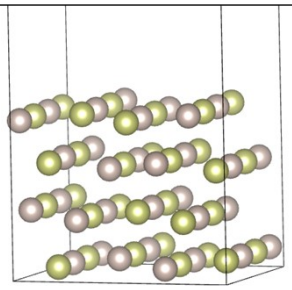	A = 10.265 Å B = 10.955 Å C = 21.592 Å α = 90° β = 90° γ = 105.52°
$Ir_3Ru_1(101)$	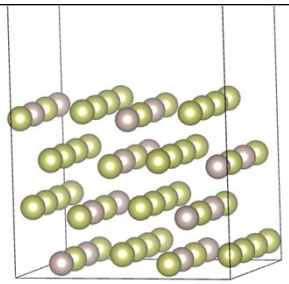	A = 10.367 Å B = 10.972 Å C = 21.623 Å α = 90° β = 90° γ = 105.35°
Ir (101)	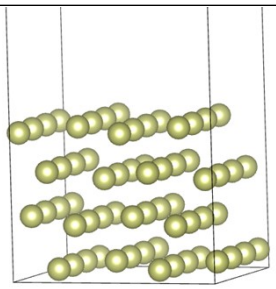	A = 10.476 Å B = 10.993 Å C = 21.649 Å α = 90° β = 90° γ = 105.21°

Table S6. Comparison of OER performance in acid.

Sample	Potential (V vs. RHE) @ 10 mA/cm^2	Current density @ 1.45 V vs. RHE	Current density @ 1.5 V vs. RHE	Stability @ 10 mA/cm^2	Catalyst loading amount μg/cm^2	V vs. RHE @ 2 h	Ref.
Ir_1Ru_4/TiC	1.465	4.3	45	2.5 mV/h	100	1.465	This work
Au@$AuIr_2$	1.55	0.4	2.05	3.35 mV/h	60	1.57	[6]
Defect rich RuO_2	1.44	20		8.3 mV/h	125	1.47	[7]
Ir-NSG	1.5	2.5	12		22		[8]
IrW alloy	1.535	0.35	2	0.25 mV/h	41.25	1.57	[9]
IrO_2/TiN	1.535		4		77.5	1.64	[10]
Ru_1/PtCu	1.46	8	48	2.1 mV/h	16.3	1.46	[11]
Ir cluster/NG	1.54		4.5	1.5 mV/h (20 mA/cm^2)	23	1.585 @20 mA	[12]
Sr_2IrO_4	1.52		6	9 mV/h	80	1.573	[13]
Co-RuIr	1.465	6.5		6 mV/h	8.9	1.59	[14]
Ru@ IrO_x	1.515	1.8	7		10	1.51	[15]
Li-IrO_x	1.53		5.5	7.5 mV/h	125	1.58	[16]
Nanoporous dtf-IrNi (From IrNiOs)	1.513						[17]
$Cr_{0.6}Ru_{0.4}O_2$	1.41	37		7 mV/h	151.05	1.44	[18]
$Ir_{0.7}Ru_{0.3}O_2$ nanoneedle	1.4 (3D)						[19]
$IrRu_4$/GKB	1.6						[20]
Ir/TiC	1.495	2.8	12	5 mV/h	227	1.52	[21]
$Y_2[Ru_{1.6}Y_{0.4}]O_{7-d}$	1.48	2.5	17		25		[22]
IrRu alloy/ $Cu_{2-x}S$ @IrS_y	1.47	7.6	35	0.3 mV/h (5 mA/cm^2)	100	1.555	[23]
IrO_x /$SrIrO_3$	1.525 @ 2 h activation	0.1	3	-1 mV/h		1.53	[24]
IrO_x /ATO	1.49		22	4 mV/h (1 mA/cm^2)	10.2	1.55	[25]

Sample	Potential (V vs. RHE) @ 10 mA/cm^2	Current density @ 1.45 V vs. RHE	Current density @ 1.5 V vs. RHE	Stability @ 10 mA/cm^2	Catalyst loading amount μg/cm^2	V vs. RHE @ 2 h	Ref.
IrO_x–Ir /C	1.52	0.3	3.5	Device, 100 h			26
IrNi @IrO_x	1.54		1.8				27
$(Na_{0.33}Ce_{0.67})_2(Ir_{1-x}Ru_x)_2O_7$	1.43						28
IrO_x core-shell				7 mV/h (1 mA/cm^2)		1.535 @1 mA	29

References

1. Muñoz, M.; Argoul, P.; Farges, F., Continuous Cauchy wavelet transform analyses of EXAFS spectra: A qualitative approach. *Am. Mineral.* **2003,** *88* (4), 694-700.
2. Muoz, M.; Farges, F.; Argoul, P., Continuous Cauchy wavelet transform of XAFS spectra. *Phys. Scr.* **2005**, 221-222.
3. Perdew, J. P.; Burke, K.; Ernzerhof, M., Generalized gradient approximation made simple. *Phys. Rev. Lett.* **1996,** *77* (18), 3865-3868.
4. Kresse, G.; Furthmuller, J., Efficient iterative schemes for ab initio total-energy calculations using a plane-wave basis set. *Phys. Rev. B Condens. Matter.* **1996,** *54* (16), 11169-11186.
5. Wang, V.; Xu, N.; Liu, J.-C.; Tang, G.; Geng, W.-T., VASPKIT: A user-friendly interface facilitating high-throughput computing and analysis using VASP code. *Comput. Phys. Commun.* **2021,** *267*, 108033.
6. Wang, H.; Chen, Z. N.; Wu, D.; Cao, M.; Sun, F.; Zhang, H.; You, H.; Zhuang, W.; Cao, R., Significantly Enhanced Overall Water Splitting Performance by Partial Oxidation of Ir through Au Modification in Core-Shell Alloy Structure. *J. Am. Chem. Soc.* **2021,** *143* (12), 4639-4645.
7. Zhao, Z. L.; Wang, Q.; Huang, X.; Feng, Q.; Gu, S.; Zhang, Z.; Xu, H.; Zeng, L.; Gu, M.; Li, H., Boosting the oxygen evolution reaction using defect-rich ultra-thin ruthenium oxide nanosheets in acidic media. *Energy Environ. Sci.* **2020**, 5143-5151.
8. Wang, Q.; Xu, C. Q.; Liu, W.; Hung, S. F.; Bin Yang, H.; Gao, J.; Cai, W.; Chen, H. M.; Li, J.; Liu, B., Coordination engineering of iridium nanocluster bifunctional electrocatalyst for highly efficient and pH-universal overall water splitting. *Nat. Commun.* **2020,** *11* (1), 4246.
9. Gao, J.; Huang, X.; Cai, W.; Wang, Q.; Jia, C.; Liu, B., Rational design of an iridium-tungsten composite with an iridium-rich surface for acidic water oxidation. *ACS. Appl. Mater. Inter.* **2020,** *12* (23), 25991-26001.
10. Zhang, K.; Mai, W.; Li, J.; Wang, H.; Li, G.; Hu, W., Highly scattered Ir oxides on TiN as an efficient oxygen evolution reaction electrocatalyst in acidic media. *J. Mater. Sci.* **2019,** *55* (8), 3507-3520.
11. Yao, Y.; Hu, S.; Chen, W.; Huang, Z.-Q.; Wei, W.; Yao, T.; Liu, R.; Zang, K.; Wang, X.; Wu, G.; Yuan, W.; Yuan, T.; Zhu, B.; Liu, W.; Li, Z.; He, D.; Xue, Z.; Wang, Y.; Zheng, X.; Dong, J.; Chang, C.-R.; Chen, Y.; Hong, X.; Luo, J.; Wei, S.; Li, W.-X.; Strasser, P.; Wu, Y.; Li, Y., Engineering the electronic structure of single atom Ru sites via compressive strain boosts acidic water oxidation electrocatalysis. *Nat. Catal.* **2019,** *2*, 304-313.

12. Wu, X.; Feng, B.; Li, W.; Niu, Y.; Yu, Y.; Lu, S.; Zhong, C.; Liu, P.; Tian, Z.; Chen, L.; Hu, W.; Li, C. M., Metal-support interaction boosted electrocatalysis of ultrasmall iridium nanoparticles supported on nitrogen doped graphene for highly efficient water electrolysis in acidic and alkaline media. *Nano Energy* **2019,** *62*, 117-126.
13. Strickler, A. L.; Higgins, D.; Jaramillo, T. F., Crystalline strontium iridate particle catalysts for enhanced oxygen evolution in acid. *ACS Appl. Energy Mater.* **2019,** *2* (8), 5490-5498.
14. Shan, J.; Ling, T.; Davey, K.; Zheng, Y.; Qiao, S. Z., Transition-metal-doped ruir bifunctional nanocrystals for overall water splitting in acidic environments. *Adv. Mater.* **2019,** *31* (17), e1900510.
15. Shan, J.; Guo, C.; Zhu, Y.; Chen, S.; Song, L.; Jaroniec, M.; Zheng, Y.; Qiao, S.-Z., Charge-redistribution-enhanced nanocrystalline Ru@IrOx electrocatalysts for oxygen evolution in acidic media. *Chem* **2019,** *5* (2), 445-459.
16. Gao, J.; Xu, C. Q.; Hung, S. F.; Liu, W.; Cai, W.; Zeng, Z.; Jia, C.; Chen, H. M.; Xiao, H.; Li, J.; Huang, Y.; Liu, B., Breaking long-range order in iridium oxide by alkali ion for efficient water oxidation. *J. Am. Chem. Soc.* **2019,** *141* (7), 3014-3023.
17. Park, S.-A.; Shim, K.; Kim, K.-S.; Moon, Y. H.; Kim, Y.-T., Enhanced activity for oxygen evolution reaction of nanoporous irni thin film formed by electrochemical selective etching process. *J. Electrochem. Sci. Technol.* **2019,** *10* (4), 402-407.
18. Lin, Y.; Tian, Z.; Zhang, L.; Ma, J.; Jiang, Z.; Deibert, B. J.; Ge, R.; Chen, L., Chromium-ruthenium oxide solid solution electrocatalyst for highly efficient oxygen evolution reaction in acidic media. *Nat. Commun.* **2019,** *10* (1), 162.
19. Faustini, M.; Giraud, M.; Jones, D.; Rozière, J.; Dupont, M.; Porter, T. R.; Nowak, S.; Bahri, M.; Ersen, O.; Sanchez, C.; Boissière, C.; Tard, C.; Peron, J., Hierarchically structured ultraporous iridium-based materials: A novel catalyst architecture for proton exchange membrane water electrolyzers. *Adv. Energy Mater.* **2019,** *9* (4), 1802136.
20. You, E.; Min, M.; Jin, S.-A.; Kim, T.; Pak, C., Highly durable, cost-effective, and multifunctional carbon-supported IrRu-based catalyst for automotive polymer electrolyte fuel cell anodes. *J. Electrochem. Soc.* **2018,** *165* (6), F3094-F3099.
21. Li, G.; Li, K.; Yang, L.; Chang, J.; Ma, R.; Wu, Z.; Ge, J.; Liu, C.; Xing, W., Boosted performance of Ir species by employing tin as the support toward oxygen evolution reaction. *ACS. Appl. Mater. Inter.* **2018,** *10* (44), 38117-38124.
22. Kim, J.; Shih, P. C.; Qin, Y.; Al-Bardan, Z.; Sun, C. J.; Yang, H., A porous pyrochlore $Y_2[Ru_{1.6}Y_{0.4}]O_{7-\delta}$ electrocatalyst for enhanced performance towards the oxygen evolution reaction in acidic media. *Angew. Chem. Int. Ed. Engl.* **2018,** *57* (42), 13877-13881.
23. Joo, J.; Jin, H.; Oh, A.; Kim, B.; Lee, J.; Baik, H.; Joo, S. H.; Lee, K., An IrRu alloy nanocactus on $Cu_{2-x}S@IrS_y$ as a highly efficient bifunctional electrocatalyst toward overall water splitting in acidic electrolytes. *J. Mater. Chem. A* **2018,** *6* (33), 16130-16138.
24. Seitz, L. C.; Dickens, C. F.; Nishio, K.; Hikita, Y.; Montoya, J.; Doyle, A.; Kirk, C.; Vojvodic, A.; Hwang, H. Y.; Norskov, J. K.; Jaramillo, T. F., A highly active and stable $IrOx/SrIrO_3$ catalyst for the oxygen evolution reaction. *Science* **2016,** *353* (6303), 1011-1014.
25. Oh, H. S.; Nong, H. N.; Reier, T.; Bergmann, A.; Gliech, M.; Ferreira de Araujo, J.; Willinger, E.; Schlogl, R.; Teschner, D.; Strasser, P., Electrochemical catalyst-support effects and their stabilizing role for irox nanoparticle catalysts during the oxygen evolution reaction. *J. Am. Chem. Soc.* **2016,** *138* (38), 12552-12563.
26. Lettenmeier, P.; Wang, L.; Golla-Schindler, U.; Gazdzicki, P.; Canas, N. A.; Handl, M.; Hiesgen, R.; Hosseiny, S. S.; Gago, A. S.; Friedrich, K. A., Nanosized IrO_x-Ir catalyst with relevant activity for anodes of proton exchange membrane electrolysis produced by a cost-effective procedure. *Angew. Chem. Int. Ed. Engl.* **2016,** *55* (2), 742-746.
27. Reier, T.; Pawolek, Z.; Cherevko, S.; Bruns, M.; Jones, T.; Teschner, D.; Selve, S.; Bergmann, A.; Nong, H. N.; Schlogl, R.; Mayrhofer, K. J.; Strasser, P., Molecular insight in structure and activity of highly efficient, low-Ir Ir-Ni oxide catalysts for electrochemical water splitting (OER). *J. Am. Chem. Soc.* **2015,** *137* (40), 13031-13040.

28. Sardar, K.; Petrucco, E.; Hiley, C. I.; Sharman, J. D.; Wells, P. P.; Russell, A. E.; Kashtiban, R. J.; Sloan, J.; Walton, R. I., Water-splitting electrocatalysis in acid conditions using ruthenate-iridate pyrochlores. *Angew. Chem. Int. Ed. Engl.* **2014,** *53* (41), 10960-10964.
29. Nong, H. N.; Gan, L.; Willinger, E.; Teschner, D.; Strasser, P., IrOx core-shell nanocatalysts for cost- and energy-efficient electrochemical water splitting. *Chem. Sci.* **2014,** *5* (8), 2955-2963.